Power uprates
and plant life extension

CASL-U-2013-0203-001

Consortium for Advanced Simulation of LWRs

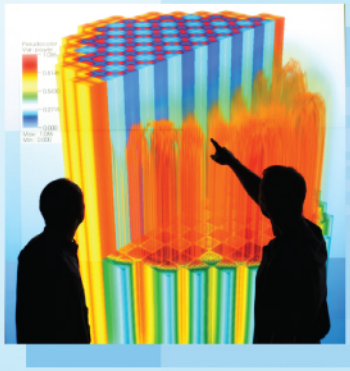

Engineering design
and analysis

Thermal Hydraulic Simulations, Error Estimation and Parameter Sensitivity Studies in Drekar::CFD

Thomas M. Smith, John N. Shadid, Roger P. Pawlowski, Eric C. Cyr and Timothy M. Wildey

Sandia National Laboratories

September, 2013

Science-enabling
high performance
computing

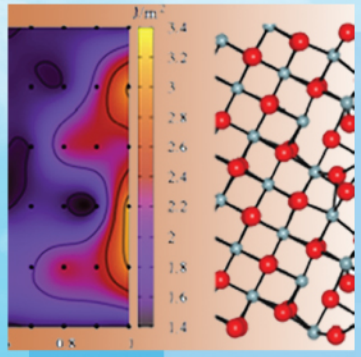

Fundamental science

Plant operational data

U.S. DEPARTMENT OF ENERGY | Nuclear Energy

SANDIA REPORT

SAND2013-XXXX
Unlimited Release
Printed September 2013

Thermal Hydraulic Simulations, Error Estimation and Parameter Sensitivity Studies in Drekar::CFD

Thomas M. Smith, John N. Shadid, Roger P. Pawlowski, Eric C. Cyr and Timothy M. Wildey

Prepared by
Sandia National Laboratories
Albuquerque, New Mexico 87185 and Livermore, California 94550

Sandia National Laboratories is a multi-program laboratory managed and operated by Sandia Corporation, a wholly owned subsidiary of Lockheed Martin Corporation, for the U.S. Department of Energy's National Nuclear Security Administration under contract DE-AC04-94AL85000.

Approved for public release; further dissemination unlimited.

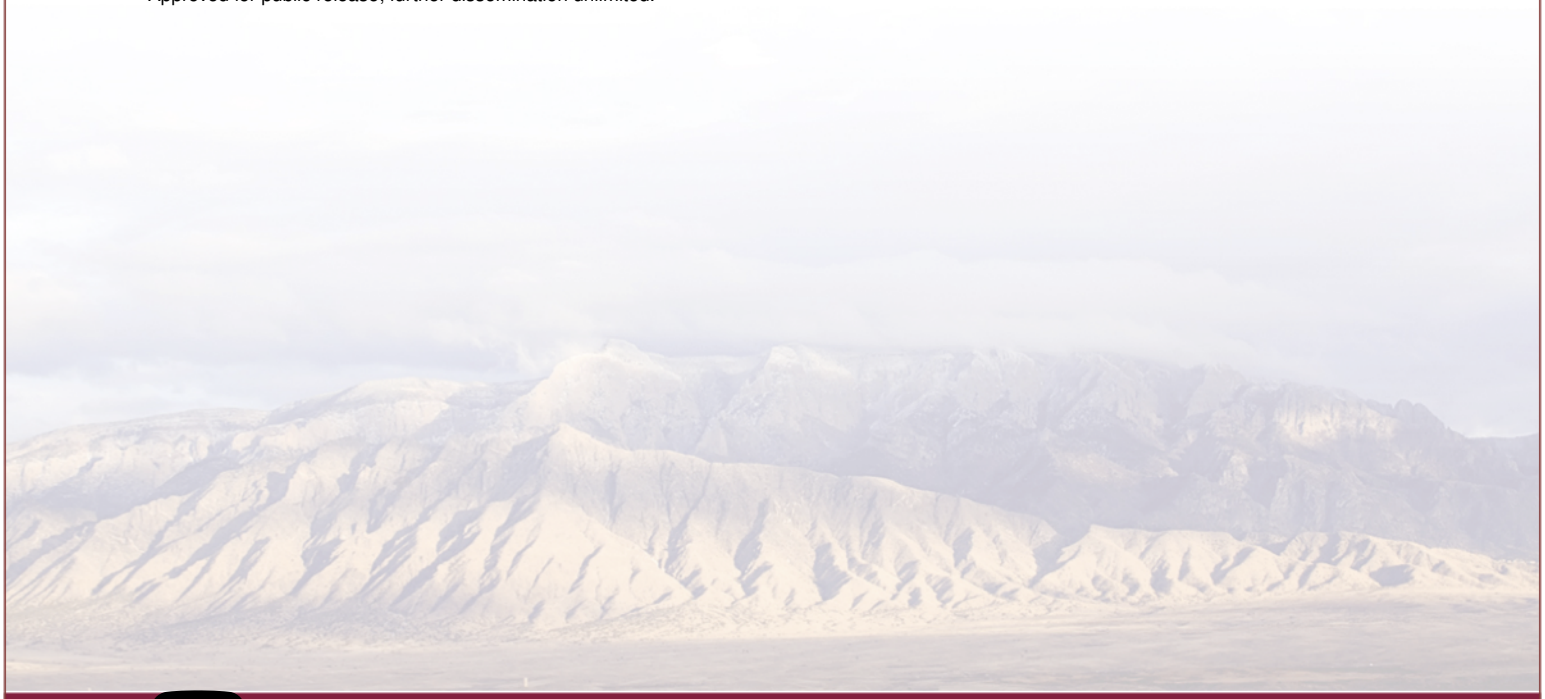

Sandia National Laboratories

CASL-U-2013-0203-001

Issued by Sandia National Laboratories, operated for the United States Department of Energy by Sandia Corporation.

NOTICE: This report was prepared as an account of work sponsored by an agency of the United States Government. Neither the United States Government, nor any agency thereof, nor any of their employees, nor any of their contractors, subcontractors, or their employees, make any warranty, express or implied, or assume any legal liability or responsibility for the accuracy, completeness, or usefulness of any information, apparatus, product, or process disclosed, or represent that its use would not infringe privately owned rights. Reference herein to any specific commercial product, process, or service by trade name, trademark, manufacturer, or otherwise, does not necessarily constitute or imply its endorsement, recommendation, or favoring by the United States Government, any agency thereof, or any of their contractors or subcontractors. The views and opinions expressed herein do not necessarily state or reflect those of the United States Government, any agency thereof, or any of their contractors.

Printed in the United States of America. This report has been reproduced directly from the best available copy.

Available to DOE and DOE contractors from
U.S. Department of Energy
Office of Scientific and Technical Information
P.O. Box 62
Oak Ridge, TN 37831

Telephone: (865) 576-8401
Facsimile: (865) 576-5728
E-Mail: reports@adonis.osti.gov
Online ordering: http://www.osti.gov/bridge

Available to the public from
U.S. Department of Commerce
National Technical Information Service
5285 Port Royal Rd
Springfield, VA 22161

Telephone: (800) 553-6847
Facsimile: (703) 605-6900
E-Mail: orders@ntis.fedworld.gov
Online ordering: http://www.ntis.gov/help/ordermethods.asp?loc=7-4-0#online

SAND2013-XXXX
Unlimited Release
Printed September 2013

Thermal Hydraulic Simulations, Error Estimation and Parameter Sensitivity Studies in Drekar::CFD

Thomas M. Smith, John N. Shadid,
Roger Pawlowski, Eric C. Cyr and Timothy M. Wildey
Sandia National Laboratories
P.O. Box 5800
Albuquerque, NM 87185-1318
tmsmith@sandia.gov, jnshadi@sandia.gov,
rppawlo@sandia.gov, eccyr@sandia.gov, tmwilde@sandia.gov

Abstract

This report describes work directed towards completion of the Thermal Hydraulics Methods (THM) CFD Level 3 Milestone THM.CFD.P7.05 for the Consortium for Advanced Simulation of Light Water Reactors (CASL) Nuclear Hub effort. The focus of this milestone was to demonstrate the thermal hydraulics and adjoint based error estimation and parameter sensitivity capabilities in the CFD code called Drekar::CFD. This milestone builds upon the capabilities demonstrated in three earlier milestones; THM.CFD.P4.02 [12], completed March, 31, 2012, THM.CFD.P5.01 [15] completed June 30, 2012 and THM.CFD.P5.01 [11] completed on October 31, 2012.

Acknowledgment

The authors thank Rick Garcia of Sandia National Laboratories for delivering Cubit based meshes of the 3x3 periodic rod/spacer grid reactor core sub-assembly model.

Contents

1 Background . . . 7
2 RANS Model for Incompressible Turbulent Flows . . . 9
3 Governing Flow Equations . . . 10
3.1 Heat Flux Vector . . . 10
3.2 Viscous Dissipation Source Term . . . 11
3.3 Turbulent Heat Flux Closure Model . . . 11
3.4 Spalart-Allmaras Eddy Viscosity Model . . . 11
3.5 Normal Distance to the Wall . . . 13
4 Computational Experiments . . . 14
4.1 LES . . . 14
4.2 Fully Developed Pipe Flow . . . 14
4.2.1 Laminar Flow . . . 14
4.2.2 Turbulent Flow . . . 16
4.3 Heat Transfer in 3x3 Rod/Spacer Grid Model . . . 22
4.4 Conjugate Heat Flow . . . 26
4.5 Embedded Uncertainty Quantification for Thermal Hydraulics . . . 29
4.5.1 Error Estimation and Adjoint Sensitivity Analysis for CFD: Fully-Developed 3D Rectangular Laminar Duct Flow . . . 31
4.5.2 Adjoint Sensitivity Analysis for CFD: 3D Turbulent Swirling Flow in Circular Expanding Pipe . . . 34
4.5.3 Error Estimation 3D Turbulent Swirling Flow in Circular Expanding Pipe . 36
5 Summary and Observations . . . 38
References . . . 40

Figures

1 Two cut-away views of the 62,000 element tube mesh [11]. . . . 16
2 Time history of total kinetic energy in the tube with the Spalart-Allmaras turbulence model [11]. . . . 17
3 Mean velocity profiles for the tube with the Spalart-Allmaras turbulence model [11]. 17
4 Law-of-the-Wall for the tube with the Spalart-Allmaras turbulence model [11]. . . . 18
5 Kays&Crawford correlations for Nu vs. Re at different Pr for fully developed turbulent pipe flow with constant heat flux wall BCs [7]. . . . 19
6 Comparisons of Nu vs. Re between Kays&Crawford [7] (eq.13-8) and Drekar for Pr=0.5,1.0,1.5, Prt=1 and constant heat flux wall BCs. . . . 20
7 Comparisons of Nu vs. Re between Kays&Crawford [7] (eq.13-8,13-9) and Drekar for Pr=1.0, Prt=0.5,0.9,1.0,2.0 and constant heat flux wall BCs. . . . 21
8 Temperature contours in 15M element 3x3 rod/spacer grid thermal fluid simulation with constant temperature wall BCs. . . . 23
9 Temperature contours in 15M element 3x3 rod/spacer grid thermal fluid simulation with constant heat flux wall BCs. . . . 23

10 Normalized SARANS eddy viscosity for 1M, 3M and 6M element meshes of 3d_10d periodic 3x3 rod/spacer grid model along center line of a sub-channel in z-direction [12]. 24
11 Temperature contours in solid rods of a 3x3 rod/spacer grid conjugate heat transfer simulation. 27
12 Temperature contours in fluid region of a 3x3 rod/spacer grid conjugate heat transfer simulation. 27
13 Temperature contours in an axial (z) plane just down stream of the mixing vanes in a 3x3 rod/spacer grid conjugate heat transfer simulation. Note a change in scale to emphasize temperature mixing. 28
14 Vx-component of velocity colored by the magnitude. 32
15 Convergence of exact error in QoI, adjoint based estimated error in QoI, and exact relative error in sensitivity. 33
16 Image of axisymmetric sudden expansion tube at steady-state conditions with $S = 0.08$. Iso-surface of z-component of velocity colored by x-component of velocity, taken from [11]. 35

Tables

1 Navier Stokes Equations. 10
2 Spalart-Allmaras RANS Turbulence Model Equation. 12
3 Model parameters for Spalart-Allmaras turbulence model. 12
4 Equation for Determining Normal-Distance-to-Wall. 13
5 Fully developed laminar pipe flow, Nu (const. heat flux), Nu (const. temperature), $Re = 10$, $Pr = 7.0$. 15
6 Fully developed turbulent pipe flow with The Spalart-Allmaras model. 19
7 Kinetic energy for the 3x3 rod/spacer grid steady-state RANS simulations using the Spalart-Allmaras turbulence model, for different mesh resolutions. 22
8 Heat flux leaving the domain for the 3x3 rod/spacer grid steady-state RANS simulations using the Spalart-Allmaras model, at different mesh resolutions. Heat flux computed with constant temperature and constant heat flux wall boundary conditions. 24
9 Variation of heat flux with Prt for the 14,994,367 element mesh. Heat flux computed with constant wall temperature and constant wall heat flux boundary conditions. 25
10 Error Estimation for CFD. 31
11 Adjoint Sensitivity Analysis for CFD. 32
12 Estimate of two QoI and adjoint sensitivity for swirling flow in axisymmetric sudden expansion tube. 35
13 Error Estimation and Adjoint Sensitivity Analysis for CFD. 35
14 Summary of computational effort of error estimation for Swirl flow with $Re_D = 10e4$ and $S = 0.04$. 36
15 Error estimation for Swirl flow with $Re_D = 10e4$ and $S = 0.04$. 37

1 Background

Full scale system level simulations of high Reynolds number flows in PWR reactors with coupled neutronics and conjugate heat transfer remain a very computationally challenging problem. Even solving the turbulent flow alone in a geometry representing only a fraction of the entire system remains a very difficult problem. For this class of problems solving the Reynolds averaged equations is currently the only feasible option for obtaining solutions. Unsteady RANS or large-eddy simulation may someday be feasible. Until then there is a great need to develop steady-state RANS models and push this methodology as far as it can be and understand the strengths and weaknesses and quantify uncertainties. For this reason RANS modeling capabilities are being developed in Drekar for the CASL program.

Our approach is to use fully implicit and fully coupled finite element methods that are very efficient for achieving steady-state solutions and for coupled multi physics simulations (e.g., turbulent flow and conjugate heat transfer). These solutions can be obtained by integrating a transient solution to steady-state with very large time steps (pseudo-time stepping), sometimes directly to steady-state and also by parameter continuation where an initial simulation at a particular parameter value (e.g., Re) is then continued to trace out an entire solution branch (see e.g., [13]). An important feature of the Drekar infrastructure is that it supports error estimation, sensitivity and uncertainty quantification (UQ) algorithms. This is in both an embedded and in a black-box mode with an existing coupling interface to DAKOTA. This technology was demonstrated in a companion VUQ milestone that carried out an initial UQ study (L3:VUQ.SAUQ.P5.02) using Drekar and two RANS models. Finally Drekar also has the potential capability to carry out parameter continuation along with bifurcation and linear stability studies as well [13].

A detailed description of Drekar is beyond the scope of this report. A theory manual was written as part of an earlier milestone and is available as a CASL archive [10]. Instead, the main ideas behind the RANS models and how they couple to the Navier-Stokes equations will be presented.

In this report the Spalart and Allmaras [17] is used. This model includes a single time dependent advection-diffusion-reaction PDE for the eddy viscosity. This viscosity couples to the Navier-Stokes equations using the Boussinesq approximation. Therefore, the stress tensor in the momentum equation is modified by an additional ”effective” viscosity.

A variation of the classic $k-\varepsilon$ two equation model, due to Lam&Bremhorst [8] has been implemented and tested (see THM.CFD.P4.02 [12]) however, serious robustness issues remain when wall damping functions are incorporated into wall bounded flow simulations. For this reason, it was not used to generate any solutions referenced in this report.

Steady-state solutions to the 3×3 rod/spacer grid problem using the Spalart-Allmaras RANS turbulence model have been demonstrated and reported on earlier in the theory manual [10] and an earlier CASL level 2 milestone report (THM.CFD.P4.02) [12]. For these solutions we were able to take time steps that grew to $CFL > 10,000$ which allowed the code to quickly integrate to 2.5 seconds of physical time.

In the remaining sections, RANS models appropriate for solving incompressible high Reynolds number flows with heat transfer are described along with the modifications to the momentum equations necessary for coupling. The milestone description contained three main tasks;

1. complete the isothermal LES of the 3x3 periodic rod/spacer grid prototype model,
2. simulate the thermal hydraulics in a prototype reactor core model and,
3. compute parameter sensitivities and error estimation of a Quantity of Interest derived from a CASL benchmark test problem.

The results are broken into three main sections that correspond to the three milestone tasks. The task (1) section is quite brief. A 12M element mesh solution was completed late CY2012 and from that solution it was determined that an additional level of refinement was necessary. However, due to availability of compute resources and interruptions to user access this refinement level has not been completed. The task (2) section first presents a validation of heat transfer by solving fully developed laminar flow in a pipe and comparing the Nusselt number to analytically derived values. This test is then repeated for fully developed turbulent pipe flow. We then present thermal hydraulic solutions for the 3x3 periodic rod/spacer grid reactor model applying constant temperature and constant wall heat flux boundary conditions. The section is concluded with a demonstration a conjugate heat transfer simulation of the same reactor core model. The task (3) section also begins with a validation of the error estimate and parameter sensitivity predictions by solving fully developed rectangular duct flow for which an analytic solution exists. The problem establishes the accuracy of the error estimates and parameter sensitivities to a quantity of interest that can also be computed analytically. The final problem investigated is the CASL benchmark problem two, steady-state swirling flow through a sudden expansion tube. Parameter sensitivity to a quantity of interest along with error estimations are computed and the accuracy inferred. We conclude with a summary of the work presented in this report.

2 RANS Model for Incompressible Turbulent Flows

In the Reynolds Averaged Navier-Stokes turbulence model methodology, a time filter is applied to the dependent flow variables resulting in the decomposition of the instantaneous velocity field into mean and fluctuating components,

$$\mathbf{u} = \bar{\mathbf{u}} + \mathbf{u}' \tag{1}$$

and produces new equations that that are very similar to the unfiltered equations with the addition of the Reynolds stress τ_t,

$$\tau_t = -\rho\overline{\mathbf{u}' \otimes \mathbf{u}'}. \tag{2}$$

This new apparent stress arises mathematically through the filter operation applied to the nonlinear advection term. It is responsible for the modification of the flow field through turbulent fluctuations. In terms of numerical simulation, it represents the "closure problem" in that additional information or equations are now required that describe τ_t in order to close the filtered system of equations making solutions possible. Given a description of τ_t, it is added to the "real" stresses in the original momentum equation, providing the necessary coupling. A common approach is to use the Boussinesq approximation where the Reynolds stresses are related to the filtered stresses through the following;

$$\tau_t = -\rho\overline{\mathbf{u}' \otimes \mathbf{u}'} \approx \mu_t[\nabla\bar{\mathbf{u}} + \nabla\bar{\mathbf{u}}^T] - \frac{2}{3}[\mu_t \nabla \cdot \bar{\mathbf{u}} + \rho k]\mathbf{I} \tag{3}$$

where μ_t is the turbulent or eddy viscosity and

$$k = \frac{1}{2}\overline{\mathbf{u}' \cdot \mathbf{u}'} = \frac{1}{2}(\overline{u'u'} + \overline{v'v'} + \overline{w'w'}) \tag{4}$$

is the turbulent kinetic energy. The last term in Equation 3 is necessary for the trace of both sides of the expression to be consistent. Now the closure problem reduces to the task of calculating the eddy viscosity and turbulent kinetic energy.

3 Governing Flow Equations

The equations governing fluid motion are the Navier-Stokes equations. These equations are listed in Table 1. They represent the conservation of mass and momentum. These equations are written in "residual" form which is typical for the discretization of these equations via the finite element method. In these equations, ρ is the density (a constant), $\overline{\mathbf{u}} = u_i,\ i = 1,2,3$ is the "Reynolds

Table 1. Navier Stokes Equations.

Governing Equations	
Continuity	$R_\rho = \nabla \cdot \overline{\mathbf{u}} = 0$
Momentum	$R_m = \rho \frac{\partial \overline{\mathbf{u}}}{\partial t} + \rho \overline{\mathbf{u}} \cdot \nabla \overline{\mathbf{u}} - \nabla \cdot \mathbf{T} - \rho \mathbf{f_i} = \mathbf{0}$
Energy	$R_T = \rho C_p \frac{\partial T}{\partial t} + \rho C_p \mathbf{u} \cdot \nabla T + \nabla \cdot \mathbf{q} + \nabla \cdot \mathbf{q_r} - \nabla \cdot \blacksquare = \mathbf{0}$

Averaged" velocity vector with index i representing Cartesian components in the (x,y,z) directions, T is temperature, C_p specific heat, $\mathbf{T}$ is the stress tensor for a Newtonian fluid;

$$\mathbf{T} = -p\mathbf{I} + \tau + \tau_t = -P\mathbf{I} + \mu_{eff}[\nabla \overline{\mathbf{u}} + \nabla \overline{\mathbf{u}}^T] - \frac{2}{3}\mu_{eff}(\nabla \bullet \overline{\mathbf{u}})\mathbf{I} \tag{5}$$

where p is the isotropic hydrodynamic pressure, μ_{eff} is the effective dynamic viscosity that can have contributions from turbulence models (e.g., $\mu_{eff} = \mu + \mu_t$), and $\mathbf{I}$ is the unity tensor. It is common practice to replace the pressure in the momentum equation with the sum of hydrodynamic pressure and turbulent kinetic energy;

$$P = p + \frac{2}{3}\rho k. \tag{6}$$

Therefore, the equations are closed by providing an estimate of the eddy viscosity and turbulent kinetic energy.

3.1 Heat Flux Vector

The heat flux vector is given by the Fourier model:

$$\mathbf{q} = -\kappa \nabla T \tag{7}$$

where κ is the coefficient of thermal conductivity which can be specified by the specific heat capacity, dynamic viscosity and Prandtl number (Pr); $\kappa = \mu C_p / Pr$.

A radiation source, $\mathbf{q_r}$, also appears in the temperature equation. For low speed flows, $\rho \mathbf{f}_i$ would induce a buoyancy force through temperature gradients that have components orthogonal to the gravity vector.

3.2 Viscous Dissipation Source Term

In the case of low speed incompressible flow, the viscous dissipation flux term $\nabla \cdot (\tau \cdot \mathbf{u})$ is written in non-conservative terms as; $\Phi = (\tau : \nabla \mathbf{u}) = \frac{1}{2}\mu \|\nabla \mathbf{u} + \nabla \mathbf{u}^T\|^2 - \frac{2}{3}\mu(\nabla \cdot \mathbf{u})^2$ and is implemented as a source term. This term is sometimes omitted from the equation.

3.3 Turbulent Heat Flux Closure Model

The averaged temperature equation contains the turbulent heat closure term, $\rho\overline{\mathbf{u}'h'}$, which includes the fluctuating enthalpy $h' = C_p T'$ and is modeled using the Boussinesq analogy;

$$\mathbf{q}_t = -\rho\overline{\mathbf{u}'h'} \approx -\kappa_t \nabla \overline{T} \tag{8}$$

where a turbulent or eddy conductivity is defined as;

$$\kappa_t = \frac{\mu_t C_p}{Pr_t} \tag{9}$$

and Pr_t is the turbulent Prandtl number.

Similar to the assumption that lead to equation 5 the total heat flux combines the laminar and turbulent contributions; ($\overline{\mathbf{q}} = \mathbf{q} + \mathbf{q_t}$). In the simulation of turbulent flows, the viscosity coefficient in the viscous fluxes is replaced with the sum of the natural and eddy viscosity ($\mu_t + \overline{\mu}$) and the heat conductivity is replaced by the sum of natural and turbulent conductivity ($\kappa_t + \overline{\kappa}$) in equations (5, 7). The turbulent Prandtl number Pr_t is also specified.

For RANS models that do not model the turbulent kinetic energy such as the Spalart-Allmaras [17] model presented below, the terms that contain turbulent kinetic energy that appear in the Favre averaged momentum and energy equations are simply neglected. The assumption being made that it is negligible compared with the total energy.

Note that an additional closure term appears in the temperature equation due to filtering the dissipation term;

$$\overline{\Phi} = \overline{\tau : \nabla \mathbf{u}} = \overline{\tau} : \nabla \overline{\mathbf{u}} + \overline{\tau' : \nabla \mathbf{u}'}. \tag{10}$$

In this equation the (:) symbol is used to represent a double contraction between two second-order tensors. The second term on the r.h.s. of equation 10 is currently being neglected.

3.4 Spalart-Allmaras Eddy Viscosity Model

The Spalart-Allmaras turbulence model equation [17] for an incompressible fluid is given in Table 2. The eddy viscosity is given by,

$$\mu_t = \rho \hat{\nu} f_{v1}. \tag{11}$$

Table 2. Spalart-Allmaras RANS Turbulence Model Equation.

$$R_{\hat{\nu}} = \rho \frac{\partial \hat{\nu}}{\partial t} + \rho \overline{\mathbf{u}} \cdot \nabla \hat{\nu} - \nabla \cdot \left(\rho \left(\frac{\nu + \hat{\nu}}{\sigma} \right) \nabla \hat{\nu} \right) - C_{b1} \rho \hat{\nu} \hat{S} + C_{w1} f_w \rho \left(\frac{\hat{\nu}}{d} \right)^2 - \frac{C_{b2} \rho}{\sigma} \left(\nabla \hat{\nu} \cdot \nabla \hat{\nu} \right) = 0$$

Functions defining the source terms and non-conservative viscous terms in the model are listed below;

$$\begin{aligned} \chi &= \frac{\hat{\nu}}{\nu} \\ f_{v1} = \frac{\chi^3}{\chi^3 + C_{v1}^3}, \quad f_{v2} = 1 - \frac{\chi}{1 + \chi f_{v1}}, \quad f_w &= g \left(\frac{1 + C_{w3}^6}{g^6 + C_{w3}^6} \right)^{1/6} \\ g = r + C_{w2}(r^6 - r), \quad r &= \frac{\hat{\nu}}{\hat{S} k^2 d^2} \\ \hat{S} = (2\Omega\Omega)^{1/2} + \frac{\hat{\nu} f_{v2}}{k^2 d^2}, \quad \Omega &= \frac{1}{2} \left(\nabla \overline{\mathbf{u}} - \nabla \overline{\mathbf{u}}^T \right) \end{aligned} \tag{12}$$

where Ω is the rotation tensor. Model parameters are listed in Table 3.

k	C_{b1}	C_{b2}	σ	C_{w1}	C_{w2}	C_{w3}	C_{v1}	C_{v2}
0.41	0.1355	0.622	2/3	$\frac{C_{b1}}{k^2} + \frac{1+C_{b2}}{\sigma}$	0.3	2.0	7.1	5.0

Table 3. Model parameters for Spalart-Allmaras turbulence model.

k is von Karman's constant, and d appearing in the source terms represents the normal distance to the wall. At a solid wall, $\mu_t = 0$, and therefore the boundary condition is, $\hat{\nu}_w = 0$. A different formula for $\hat{S}$ has been proposed in Blazek [3] that prevents it from taking a value of zero. The modified term, $\hat{S}_{mod}$, is;

$$\begin{aligned} \hat{S}_{mod} &= f_{v3} (2\Omega\Omega)^{1/2} + \frac{\hat{\nu} f_{v2}}{k^2 d^2}, \\ f_{v2} &= \left(1 + \frac{\chi}{C_{v2}} \right)^{-3} \\ f_{v3} &= \frac{(1 + \chi f_v v1)(1 - f_{v2})}{\max(\chi, 0.001)}. \end{aligned} \tag{13}$$

3.5 Normal Distance to the Wall

The Spalart-Allmaras turbulence model described above requires the normal-distance-to-wall (ndtw) to evaluate the wall damping functions. models. The technique used in Drekar is presented by Tucker [18]. A distance scalar variable is solved for from the equation listed in Table 4. It has the

Table 4. Equation for Determining Normal-Distance-to-Wall.

$R_\phi = -\nabla^2\phi - 1$

boundary condition, $\phi_w = 0$ at walls. The normal distance is then determined from

$$d = -\sqrt{\sum_{j=1,3}\left(\frac{\partial\phi}{\partial x_j}\right)^2} \pm \sqrt{\sum_{j=1,3}\left(\frac{\partial\phi}{\partial x_j}\right)^2 + 2\phi} \tag{14}$$

and equals the minimum absolute value of the two choices. In Drekar::CFD, this equation is solved once as a pre-processing step. The solution is then read from file at the initiation of the fluid solve.

4 Computational Experiments

4.1 LES

The Large Eddy Simulation of periodic 3x3 spacer/rod 3d_10d model has been summarized in a NURETH-14 conference paper [14], a level 2 CASL THM CFD milestone report (THM.CFD.P4.02) [12], and a CASL senior scientific leadership team site review at Sandia National Laboratories December, 17, 2012 [16]. These reports contains LES ranging from 672K up to 12M element meshes. These simulations were difficult to complete due to the job queuing system on Jaguar/Titan that only allows 12 hours of continuous execution.

Time averaged statistics such as the pressure drop across the spacer grid, turbulence intensity and eddy viscosity plotted along the center line of a sub-channel, and the total kinetic energy were trending towards grid convergence but it was also clear that additional refinement was necessary.

A stretch goal associated with the LES task of the present milestone was to run a 24M element mesh simulation. This simulation was started in the second half of CY2012. Nearly 0.25 sec. (seven flow through times) has been completed. It was being run on Jaguar/Titan using 8,912 cores. However, do to insufficient computational resources and interruptions in user access to the machine, this simulation has not been completed. Therefore, no new information of significance has been generated for this report.

4.2 Fully Developed Pipe Flow

Kays&Crawford [7] have derived expressions for the Nusselt number for fully developed pipe flow both laminar and turbulent. For laminar flow theoretical values for constant wall temperature and constant heat flux wall boundary conditions have been derived. This is a very good thermal hydraulic test case. In this section, we review the procedure for computing Nu for fully developed pipe flow and compare the analytic and semi-analytic values from Kays&Crawford [7] with computed values from Drekar solutions.

4.2.1 Laminar Flow

Consider fully developed flow in a three-dimensional circular pipe. The flow is considered fully developed when the radial velocity profile does not change with axial location in the pipe. This condition can be achieved through periodic inflow-outflow boundary conditions and a momentum source term driving the flow in the axial direction.

The Nusselt number is defined as;

$$Nu = \frac{hD}{\kappa} \tag{15}$$

where h is the local convection heat transfer coefficient, D is is a reference length scale which in this case is the pipe diameter and κ is the thermal conductivity coefficient. The mean temperature or mixing temperature T_m is the average temperature of a cross-section of the pipe and is defined as;

$$T_m = \frac{1}{\rho V A} \int_A \rho \mathbf{u} \cdot \mathbf{n} T dA \tag{16}$$

where A is the cross-sectional area, V is the average axial component of velocity defined as;

$$V = \frac{1}{\rho A} \int_A \rho \mathbf{u} \cdot \mathbf{n} dA \tag{17}$$

and $\mathbf{u}$ is the velocity vector at a point on the integration surface and $\mathbf{n}$ is a unit vector normal to the surface. Newton's law of cooling can be stated as;

$$\dot{q}''_w = h(T_w - T_m) \tag{18}$$

where $\dot{q}''_w$ is the wall heat flux. The wall heat flux is defined as;

$$\dot{q}''_w = \frac{1}{L} \oint_L \kappa \frac{\partial T}{\partial \mathbf{n}} dl. \tag{19}$$

In this case $\frac{\partial T}{\partial \mathbf{n}}$ is the temperature gradient normal to the wall and tangent to the surface for which the flux is computed and the integration is a line traversing the circumference of the tube. In a similar way, the local (axial location) reference wall temperature is computed as;

$$T_w = \frac{1}{L} \oint_L T dl. \tag{20}$$

The final definition of Nu is;

$$Nu = \frac{hD}{\kappa} = \frac{\dot{q}''_w D}{\kappa(T_w - T_m)}. \tag{21}$$

The analytic values of Nusselt number for fully developed laminar pipe flow for constant wall heat flux and constant temperature are presented in Table 5 along with predictions using Drekar::CFD. The percent difference between analytic and numerical values are also shown. For this large Prandtl

	Nu (const. $\dot{q}''_w$)	Nu (const. T)
K&C	4.364	3.658
Drekar	4.430	3.682
%Δ	1.5%	0.6%

Table 5. Fully developed laminar pipe flow, Nu (const. heat flux), Nu (const. temperature), $Re = 10$, $Pr = 7.0$.

number, the near wall resolution is seven times greater for the thermal boundary layer than for the

momentum boundary layer. Therefore, a very fine mesh was used to capture the thermal boundary layer. The Drekar solutions ($Pr = 7$, $Re_D = 10$) were obtained by solving direct-to-steady-state on a mesh containing 344,064 elements. The tube diameter is ($D = 0.01\ m$). Two views of a typical computational mesh are shown in Figure 1 which are reproduced from an earlier CASL level 2 THM CFD milestone report [11]. In these simulations, the inflow velocity profile and initial

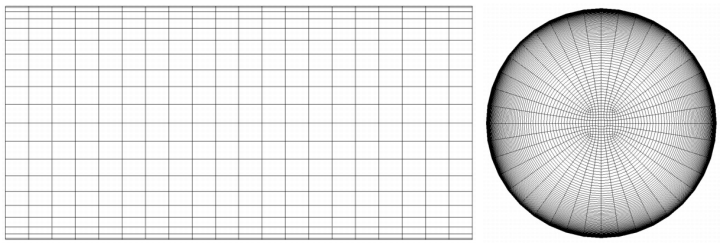

Figure 1. Two cut-away views of the 62,000 element tube mesh [11].

conditions are parabolic with respect to the radius. These conditions correspond to the analytic solution for velocity. The inflow temperature is constant and so the thermal boundary layer grows in the downstream direction. The Nusselt number is derived assuming a fully developed velocity field and temperature. Therefore, a thermal entry length is defined as the distance required for the temperature boundary layer to reach a point where the cross-section profile no longer varies with stream-wise location. Kays&Crawford derive the thermal entry length for laminar flow as;

$$\frac{x}{D} = 0.05\ Pr\ Re_D \tag{22}$$

for both constant temperature and constant heat flux wall boundary conditions. For the conditions presented here, $\frac{x}{D} = 3.5$. The computational domain was $x = 20D$ and Nu was computed at $x = 10D$.

4.2.2 Turbulent Flow

We now consider heat transfer from the wall in fully developed turbulent pipe flow. This situation is again realized by applying periodic inflow-outflow boundary conditions and a momentum source in the axial direction. This problem was studied in an earlier CASL THM CFD level 2 milestone report [11]. In that report, the law of the wall given by;

$$U^+ = \frac{1}{0.41} ln(y^+) + 5.2 \tag{23}$$

was reproduced using the Spalart-Allmaras RANS turbulence model. We summarize the results from that report in the following Figures; 2, 3 and 4 which show the time-stepping to steady-state history, mean velocity profiles and comparison of computational results to the theoretical law of

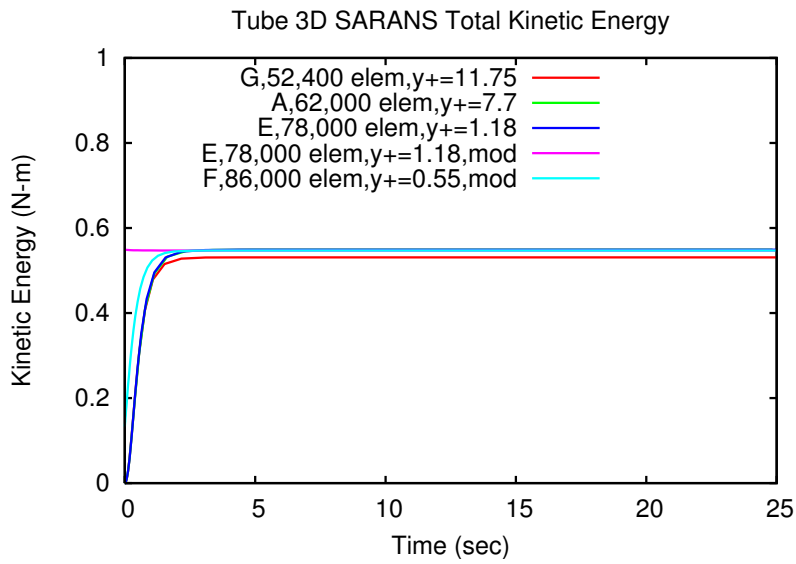

Figure 2. Time history of total kinetic energy in the tube with the Spalart-Allmaras turbulence model [11].

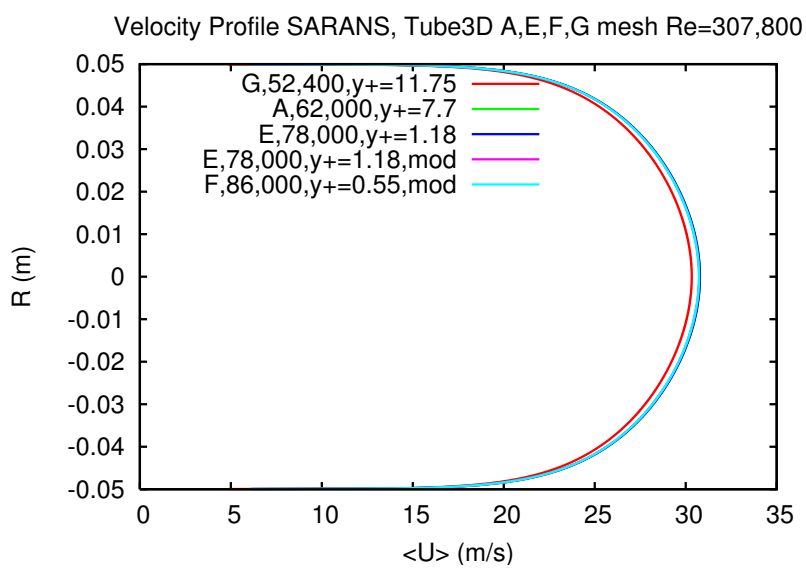

Figure 3. Mean velocity profiles for the tube with the Spalart-Allmaras turbulence model [11].

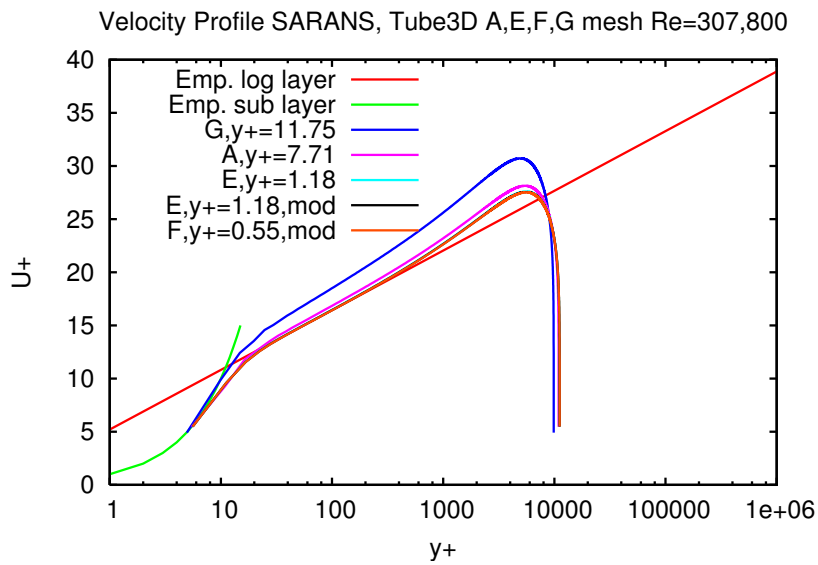

Figure 4. Law-of-the-Wall for the tube with the Spalart-Allmaras turbulence model [11].

the wall respectively. These results show that given adequate near wall resolution ($y^+ \leq\approx 10$) the non-dimensional velocity profile (law of the wall) is accurately reproduced.

For the case of fully developed turbulent pipe flow, the time averaged velocity profile can be approximated by a one-seventh power law. For Prandtl number near unity, Reynolds analogy states that the temperature profile will be similar to the velocity profile [7], thus,

$$\frac{\bar{u}}{\bar{u}_c} = \left(1 - \frac{r}{r_w}\right)^{1/7} \qquad \frac{\bar{T} - T_w}{\bar{T}_c - T_w} = \left(1 - \frac{r}{r_w}\right)^{1/7}. \tag{24}$$

Using this assumption, Kays&Crawford [7] derived a Nusselt number based on the mean velocity and temperature profiles (13-8);

$$Nu = \frac{0.152\, Re_D^{0.9}\, Pr}{0.833[2.25\ln(0.114\, Re_D^{0.9}) + 13.2Pr - 5.8]} \tag{25}$$

and for Prandtl number in the range (0.5-1.0), a simpler expression was derived (13-9);

$$Nu = 0.022\, Pr^{0.5}\, Re_D^{0.8} \qquad Re_D < 10^5. \tag{26}$$

These two formulas expressing Re_D vs. Nu are plotted in Figure 5. The thermal entry length for turbulent flow is much longer than the laminar case. It is estimated from Kays&Crawford that for $\frac{x}{D} = 20$, the error in Nu is approximately 2% ([7] p. 264). Drekar::CFD simulations were conducted using the Spalart-Allmaras RANS turbulence model. Nusselt numbers were computed to compare with these two expressions. The computational mesh contained 167,936 elements. The

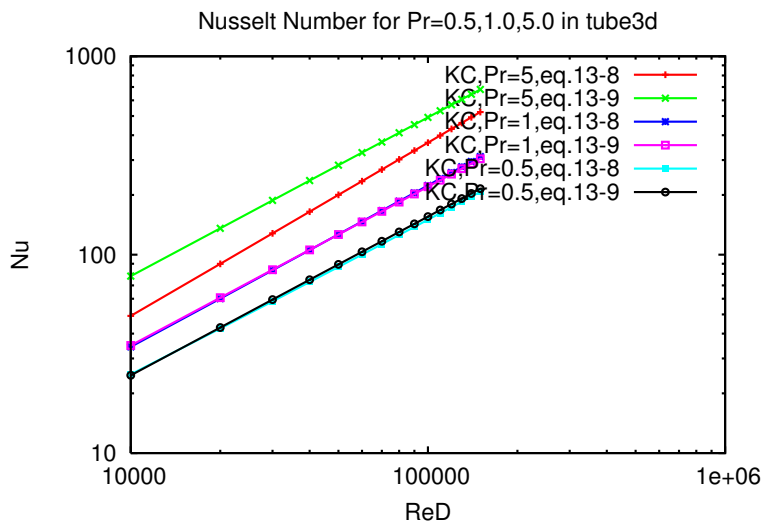

Figure 5. Kays&Crawford correlations for Nu vs. Re at different Pr for fully developed turbulent pipe flow with constant heat flux wall BCs [7].

Re_D	y^+	Δy_{min}	U_z max.
24,800	1.69	1.513e-5	2.48
53,300	3.39	1.513e-5	5.33
113,900	6.71	1.513e-5	11.39

Table 6. Fully developed turbulent pipe flow with The Spalart-Allmaras model.

Reynolds number varied from 24,800-113,900, Pr varied from 0.5-1.5 and Prt varied from 0.5-2.0. A summary of the flow conditions is contained in Table 6. Re_D vs. Nu plots for variable Pr and constant Prt are shown in Figure 6. Re_D vs. Nu plots for constant Pr are shown in 7. The predictions predict the correct slope but are shifted due to the influence of Prt. The computations show that for Prt=1, the predictions improve as Pr increases. The computations also show that the Prt lies somewhere between 0.5 and 0.9.

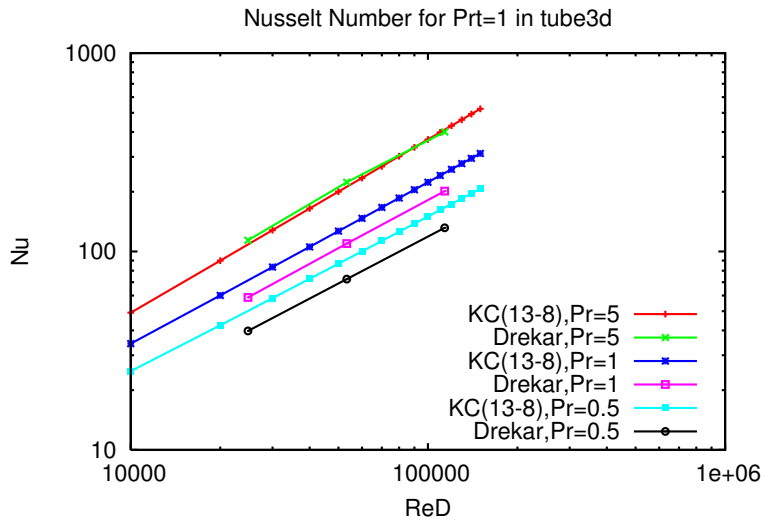

Figure 6. Comparisons of Nu vs. Re between Kays&Crawford [7] (eq.13-8) and Drekar for Pr=0.5,1.0,1.5, Prt=1 and constant heat flux wall BCs.

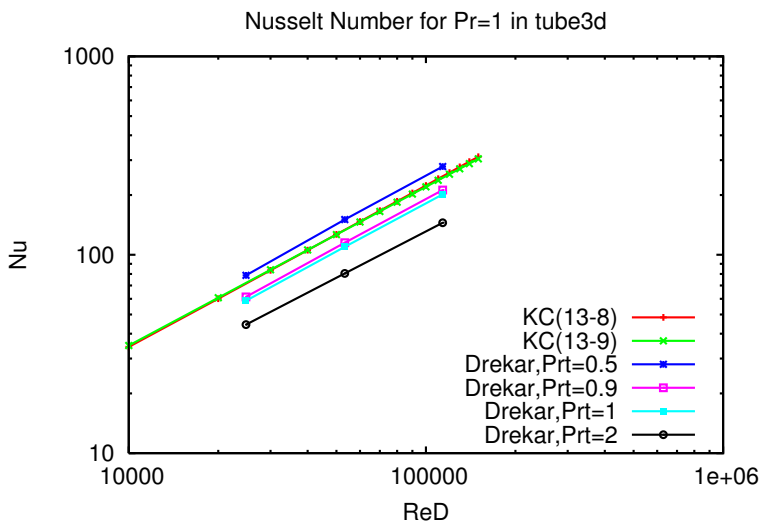

Figure 7. Comparisons of Nu vs. Re between Kays&Crawford [7] (eq.13-8,13-9) and Drekar for Pr=1.0, Prt=0.5,0.9,1.0,2.0 and constant heat flux wall BCs.

4.3 Heat Transfer in 3x3 Rod/Spacer Grid Model

In this section, we discuss results from steady-state RANS thermal hydraulic simulations of the periodic 3x3 rod/spacer grid model. The mesh geometry spanned three diameters upstream of the spacer leading edge and 25 diameters downstream of the spacer trailing edge. The inflow velocity was $U_z = 5\ m/s$. The rod diameter was $D = 0.0095\ m$. The flow properties were; density ($1\ kg/m^3$), dynamic viscosity ($2.462845e-7\ kg/ms$), heat capacity ($1\ J/(kg\ K)$), thermal conductivity ($1.69851e-7\ W/(m\ K)$) resulting in $Re_D = 192,800$ and $Pr = 1.45$. The Spalart-Allmaras, turbulence model was used in these simulations. The turbulent Prandtl number was varied from 0.5 - 1.5. The inflow temperature was ($1\ K$). Two different wall boundary conditions were investigated; constant wall temperature ($T_w = 5\ K$) and constant heat flux ($\dot{q}''_w = -0.1\ W/m^2$).

Four simulations using different mesh resolutions were run. The flow solution was first solved by time marching pseudo-transient to steady-state without solving the energy equation. And then in a separate execution, the temperature equation was solved by either pseudo-transient or direct-to-steady-state with the flow solution supplied as data. The largest mesh, with 14,994,367 elements was initiated by taking the mesh containing 1,874,296 and uniformly refining both mesh and solution. The geometry was not changed by refinement. In Table 7 the mesh sizes and total kinetic energy of the steady-state solutions are presented. The percent difference between a mesh and the next finer mesh are computed. The kinetic energy is monotonically with mesh refinement. Temperature contours on the center rod and at ten axial (z) planes for constant temperature and

Elements	TKE/vol.	%Δ
1,874,296	12.61645	xxxx
3,879,436	12.87866	2.02
8,301,944	13.09879	1.70
14,994,367	13.14279	0.30

Table 7. Kinetic energy for the 3x3 rod/spacer grid steady-state RANS simulations using the Spalart-Allmaras turbulence model, for different mesh resolutions.

constant heat flux wall boundary conditions are shown in Figures 8 and 9 respectively. In both cases, rapid mixing just beyond the mixing vanes is evident and the temperature distribution is becoming more homogeneous. The difference between the total heat flux leaving the domain and the heat flux entering the domain was computed for each of the four mesh resolutions and both wall boundary conditions. Table 8 shows the heat flux along with the y^+ and the total eddy viscosity in the computational domain normalized by the kinematic viscosity. While these results to not establish mesh convergence, and all four meshes are rather coarse based on y^+, the quantities are monotonically changing so trends can be established. A comparison of heat fluxes for a given mesh for the two different boundary conditions is not really meaningful since the wall temperature and the wall heat flux were chosen arbitrarily.

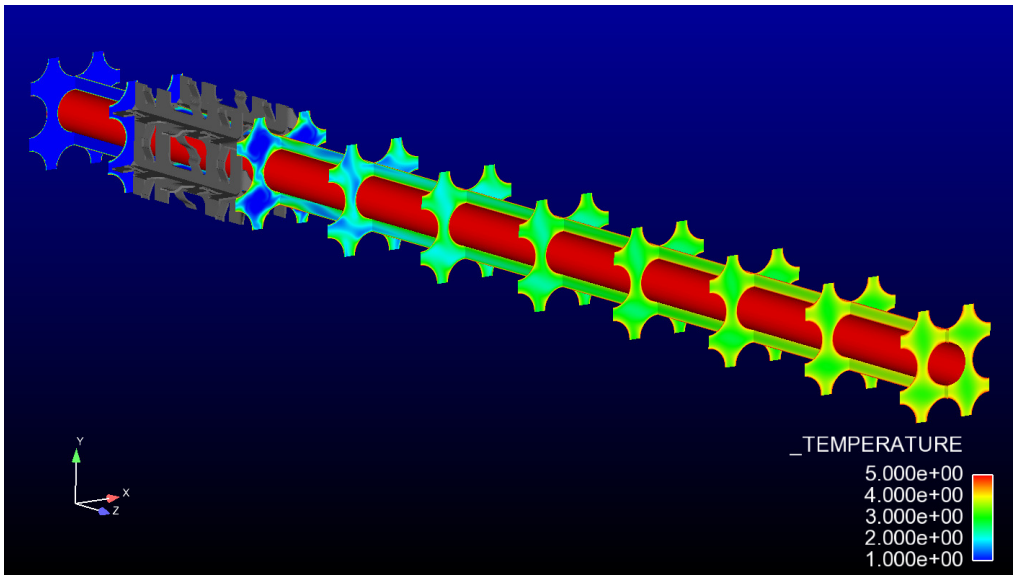

Figure 8. Temperature contours in 15M element 3x3 rod/spacer grid thermal fluid simulation with constant temperature wall BCs.

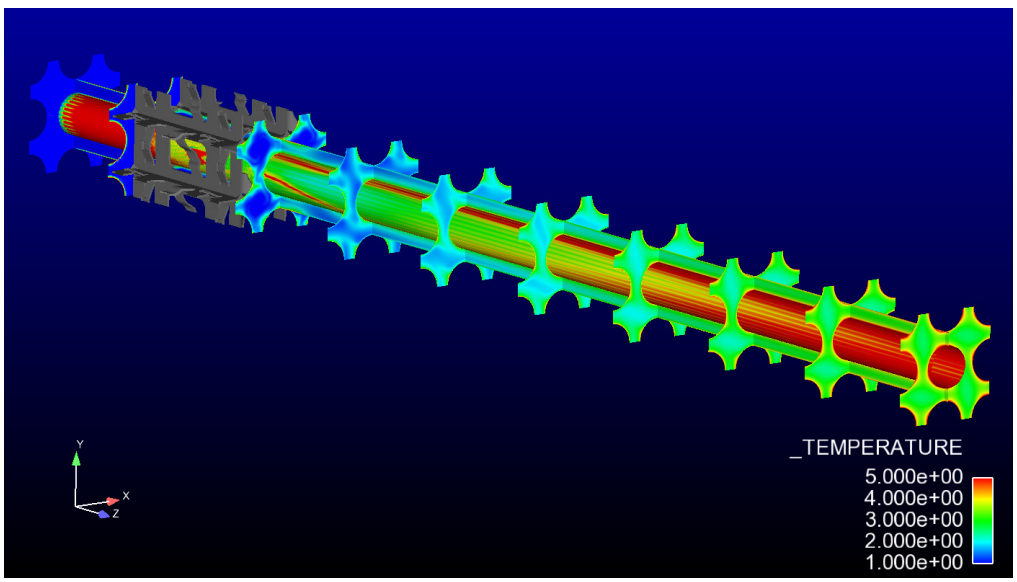

Figure 9. Temperature contours in 15M element 3x3 rod/spacer grid thermal fluid simulation with constant heat flux wall BCs.

Interestingly, though, is the trend towards a lower heat flux as the resolution increases. This may be due to a reduction in the amount of eddy viscosity in the system. As can be seen from

Table 8, the total eddy viscosity goes down with increasing mesh resolution. This same trend can be seen in Figure 10 which is reproduced from an earlier CASL level 2 milestone report (THM.CFD.P4.02) [12]. In this Figure, the eddy viscosity is plotted for three different solutions having different mesh resolutions along the center of a sub-channel of the same model geometry as the one used in the current simulations. The eddy viscosity is computed using the Spalart-Allmaras RANS model. The eddy viscosity is less for the higher resolution mesh solution.

Elements	y^+	Total $\hat{\nu}_t/\nu$	H (const $\dot{q}''$)	H (const. T)
1,874,296	66	453.947	2.418	2.691
3,879,436	54	426.666	2.165	2.687
8,301,944	47	409.065	2.160	2.645
14,994,367	44	382.678	2.130	2.514

Table 8. Heat flux leaving the domain for the 3x3 rod/spacer grid steady-state RANS simulations using the Spalart-Allmaras model, at different mesh resolutions. Heat flux computed with constant temperature and constant heat flux wall boundary conditions.

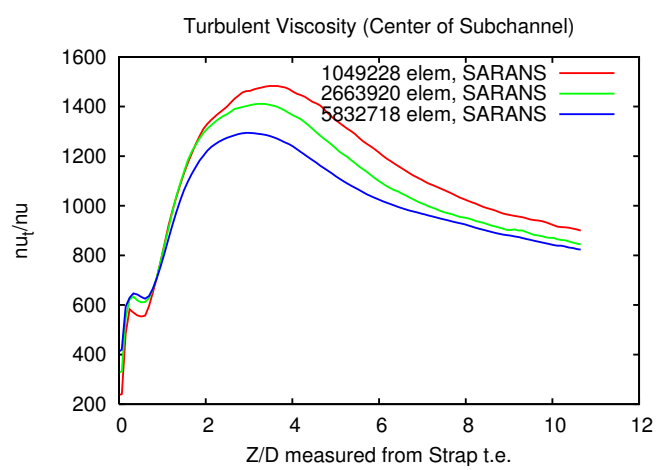

Figure 10. Normalized SARANS eddy viscosity for 1M, 3M and 6M element meshes of 3d_10d periodic 3x3 rod/spacer grid model along center line of a sub-channel in z-direction [12].

Using the flow solution for the finest mesh, Prt was varied from 0.5 - 1.5 and the difference in heat flux leaving the domain and heat flux entering the domain was computed for both wall boundary conditions. Table 9 shows that the heat flux is indeed sensitive to Prt and that higher Prt, the less heat exchanged to the fluid.

Prt	H (const $\dot{q}''$)	H (const. T)
0.5	2.155	3.270
1.0	2.130	2.514
1.5	2.091	2.055

Table 9. Variation of heat flux with *Prt* for the 14,994,367 element mesh. Heat flux computed with constant wall temperature and constant wall heat flux boundary conditions.

4.4 Conjugate Heat Flow

Drekar::CFD is a mult-physics solver. Two or more different systems of equations representing two or more different physical models can be solved in a tightly coupled way. An example of this is conjugate heat transfer between solid rods in a reactor core and water contained in the reactor vessel. In this section conjugate heat transfer is demonstrated using the same reactor model geometry for the fluid domain as discussed above for 3x3 rod/spacer thermal hydraulics problem. The total mesh contained 2,601,044 elements. The fluid mesh contained 1,391,936 element and the solid mesh contained 1,209,108 elements.

The inflow velocity was ($U_z = 5\ m/s$). The fluid properties were; density ($943\ kg/m^3$), dynamic viscosity ($2.3e-3\ kg/ms$), heat capacity ($4248\ J/kgK$) and thermal conductivity ($6.879\ W/mK$) resulting in $Pr = 1.42$ and $Re_D = 192,800$. The turbulent Prandtl number was specified as $Prt = 0.9$.

The solid material properties for the fuel pellets and the cladding were assumed to be equal to Zirconium; density ($6570\ kg/m^3$), heat capacity ($278\ J/kgK$) and thermal conductivity ($12.4\ W/mK$).

The conjugate solid-fluid problem ran on Titan using 4096 cores until roughly two flow through times were simulated ($\approx 0.11722\ sec.$). At this point the flow was approximately steady-state, however, the temperature in the solid and fluid were not in balance. Since the temperature equations are linear with respect to the flow variable, the two temperature equations can be solved simultaneously by prescribing the flow variables as data. This is a much more efficient way to achieve a steady-state condition. The solid-fluid temperature equations were solved by pseudo transient to steady-state using 256 cores, and took only 498 sec. and 74 time steps to reach 25 sec. of computational time.

A constant volumetric source term, ($1.0e8\ J/m^3s$), produced an increase in temperature from 120 K to 175 K in the rods. The maximum temperature in the fluid is 138 K. Temperature contours in the solid rods are shown in Figure 11. The rods are hottest at the center and cool radially due to heat transfer to the fluid. Temperature contours on the surface of the center rod and on five axial (z) planes are shown in Figure 12. Figure 13 shows an axial plane (z) of the temperature solution just down stream from the mixing vanes. The contour scale was changed to emphasize temperature mixing. Mixing due to swirl is evident.

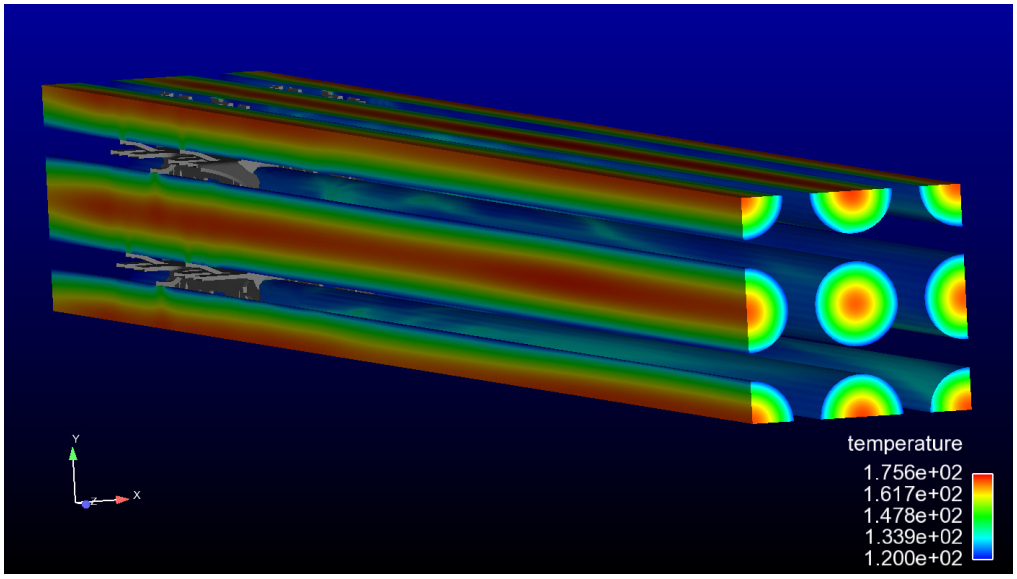

Figure 11. Temperature contours in solid rods of a 3x3 rod/spacer grid conjugate heat transfer simulation.

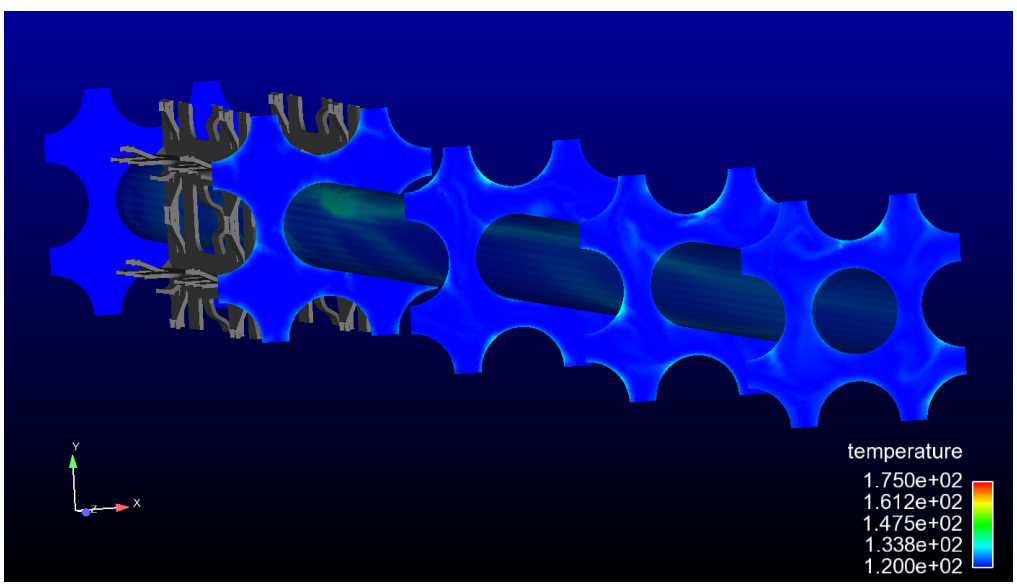

Figure 12. Temperature contours in fluid region of a 3x3 rod/spacer grid conjugate heat transfer simulation.

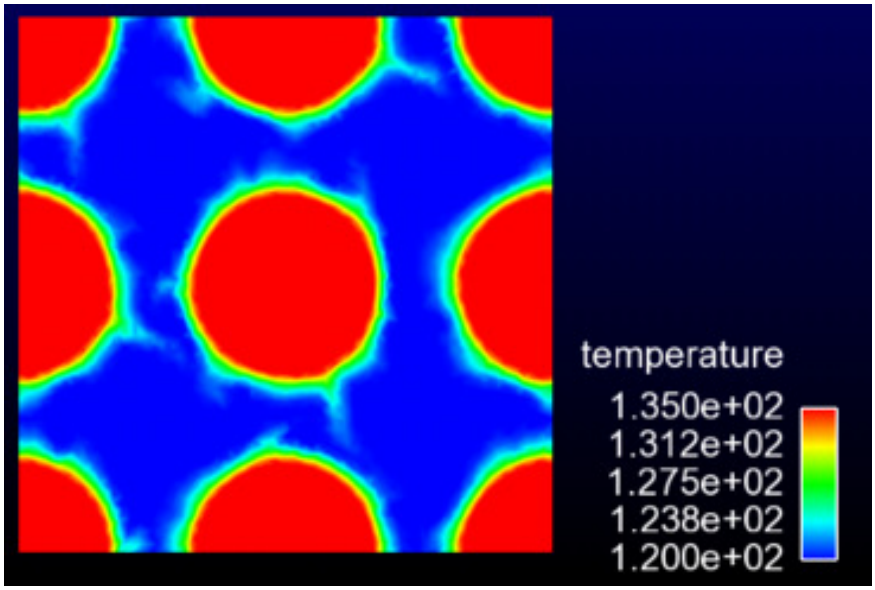

Figure 13. Temperature contours in an axial (z) plane just down stream of the mixing vanes in a 3x3 rod/spacer grid conjugate heat transfer simulation. Note a change in scale to emphasize temperature mixing.

4.5 Embedded Uncertainty Quantification for Thermal Hydraulics

In this section we describe the use of embedded algorithms to estimate errors in a given Quantity of Interest (QoI), compute parameter sensitivities and construct a linear surrogate model for UQ based upon computed sensitivity in two CFD simulations. The first simulation is fully developed steady laminar flow in a rectangular duct, for which an analytic solution exists. The second simulation is steady-state turbulent flow through an axisymmetric sudden expansion duct using the Spalart-Allmaras RANS turbulence model. The algorithms embedded in Drekar::CFD make use of the same operators and tools that are used to solve the forward problem, namely, Jacobian matrix operator, weak residual operator, and automatic differentiation. Several CASL VUQ milestones related to this work have been completed (L3.VUQ.SAUQ.P5.05) [19], (L3.VUQ.SAUQ.P6.01) [20], and a detailed description of this approach can be found in [4]. In these milestone reports, the derivation of adjoint based error estimation using Drekar::CFD were discussed and several examples including steady-state turbulent flow simulations using the Spalart-Allmaras model were presented. In this report, parameter sensitivities and a straight forward application to UQ are also included. For a detailed explanation, the reader is referred to the above cited documents.

Predictive computational analysis and uncertainty quantification (UQ) for multi physics has many open challenges including; uncertainties arising from: discretization errors, boundary and initial conditions, model parameters and physical parameters. Analysis and design often focus on a set of quantities of interest (QoI) rather than the entire state (e.g. partial differential equation (PDE) solution). The stability, error, uncertainty propagation and sensitivity characteristics for QoI can be significantly different from the PDE solution itself.

We are addressing these challenges for studies of a moderate number of QoIs dependent on a large-number of parameters using fully coupled Newton-Krylov methods and embedded adjoint-based methods to accurately and efficiently compute numerical error estimates and to conduct sensitivity analysis for QoI. Adjoint methods have been well studied and demonstrated for systems of PDEs (see; Bangerth&Rannacher [1], Becker [2], Eriksson et al. [5], Estep et al. [6]).

An algorithm for computing error estimates for a Quantity-of-Interest (QoI) is presented next (taken from [19]). Given low and high order approximation spaces V_L and V_H respectively. We will refer to low- and high-order approximations which typically correspond to linear and quadratic basis approximations respectively. Let the weak solution to a system of PDEs be denoted by,

$$\mathbf{f}(\mathbf{z}_L, \mathbf{v}_L) = 0 \quad \forall \mathbf{v}_L \in \mathbf{V}_L \tag{27}$$

which is achieved by repeated iterations of Newton's method,

$$\mathbf{J}\Delta\mathbf{z}_L = -\mathbf{f}(\mathbf{z}_L, \mathbf{v}_L) \tag{28}$$

where $\mathbf{z}_L$ is a "low" order approximation to the continuous solution and $\mathbf{v}_L$ is a low order weight function, $\mathbf{J}(\mathbf{z}_L, \mathbf{v}_L)$ is the Jacobian matrix, $\Delta\mathbf{z}_L$ is the solution update to $\mathbf{z}_L$ and $\mathbf{f}$ is the residual vector. Define a QoI as:

$$\mathbf{\Psi}_H = (\mathbf{\Psi}, \mathbf{v}_H) \quad \forall \mathbf{v}_H \in \mathbf{V}_H. \tag{29}$$

(1) Project the low-order approximation onto a higher-order basis:

$$\mathscr{P}(\mathbf{z}_L) = \mathbf{z}_H. \tag{30}$$

(2) Compute a high-order residual:

$$\mathbf{r}_H = -\mathbf{f}(\mathbf{z}_H, \mathbf{v}_H) \quad \forall \mathbf{v}_H \in \mathbf{V}_H. \tag{31}$$

Remark

Unlike eq. 27 where Galerkin orthogonality exists, the residual is not necessarily equal to zero in the higher-order function space.

(3) Form a high-order Jacobian linearized about the projected high-order solution:

$$\mathbf{J}_H(\mathbf{z}_H, \mathbf{v}_H) \quad \forall \mathbf{v}_H \in \mathbf{V}_H. \tag{32}$$

(4) Solve the adjoint problem:

$$\mathbf{J}_H^T \boldsymbol{\phi}_H = \boldsymbol{\Psi}_H. \tag{33}$$

(5) Finally, estimate the error in the QoI from:

$$(\boldsymbol{\Psi}, \mathbf{e}) = (\mathbf{r}_H, \boldsymbol{\phi}_H). \tag{34}$$

Remark

The transpose may represent taking the strong-form adjoint (see [4] for more discussion).

As an example, $\boldsymbol{\Psi} = \frac{\partial \mathbf{g}}{\partial \mathbf{z}}$ where g is determined from,

$$g(\mathbf{z}) = \int_\Omega \mathbf{z} \delta d\Omega. \tag{35}$$

In this functional, δ has a value of one inside a prescribed box and zero outside the box. In some cases, the QoI is a boundary term such as heat flux from the wall, or lift or drag of an immersed object.

(6) Compute sensitivity: Sensitivity in the QoI ($g(\mathbf{z}(\lambda))$) now parametrized by (λ), is estimated using the same algorithm described above only replacing eq. 34 with;

$$\frac{dg}{d\lambda} = \left(\boldsymbol{\Psi}, \frac{\partial \mathbf{r}}{\partial \lambda} \right). \tag{36}$$

Remark

The adjoint sensitivity can be entirely computed from a low order approximation making the projection, eq. 30 un-necessary and the adjoint problem low-order.

4.5.1 Error Estimation and Adjoint Sensitivity Analysis for CFD: Fully-Developed 3D Rectangular Laminar Duct Flow

In this first example of adjoint based error estimation and sensitivity analysis the fully developed steady laminar flow in a rectangular cross-sectional duct is simulated. For this problem, an analytic solution exists,

$$u(y,z) = \frac{16a^2}{\mu\pi^3}(-\frac{\partial p}{\partial x}) \sum_{i=1,3,5,\ldots}^{\infty} (-1)^{(i-1)/2} \left[1 - \frac{cosh(i\pi z/2a)}{cosh(i\pi b/2a)}\right] . \frac{cos(i\pi y/2a)}{i^3} \tag{37}$$

For a QoI, the average fluid x-component of velocity (Vx) is chosen;

$$\bar{V} = \int_{-a}^{a}\int_{-b}^{b} V_x \, dydz. \tag{38}$$

An analytic solution for the QoI also exists,

$$\bar{V} = \frac{a^2}{3\mu}(-\frac{\partial p}{\partial x}) \left[1 - \frac{192a}{\pi^5 b} \sum_{i=1,3,5,\ldots}^{\infty} \frac{tanh(i\pi b/2a)}{i^5}\right] . \tag{39}$$

The reference solution was computed using 15 terms in the series. The forward solution was approximated using SUPG with Q1 elements and the adjoint equation was solved with Q2 elements. Simulations were conducted with a $Nx \times Ny \times Nz = 100 \times 40 \times 40$ element mesh. Solutions were computed at four Reynolds numbers $Re = \frac{\rho V L}{\mu}$ and the solutions were obtained by starting from a trivial initial guess with a direct-to-steady-state solution procedure. Parameters in this simple numerical sensitivity study were dynamic viscosity and pressure gradient (μ, G_0) respectively. Figure 14 shows a surface colored by magnitude of x-component of velocity. Table 10 shows a comparison between the exact QoI and the Drekar predicted QoI and the adjoint based error estimate for four Reynolds number solutions. The fourth column is the ratio of the adjoint based error estimate and the true error (difference between exact and Drekar predicted QoI). Table 11 compares the sensitivity of the QoI to the viscosity and pressure at the four Reynolds number solutions. The exact sensitivity is obtained by differentiating the analytical solution (Eq. 39) of the QoI with respect to either viscosity or pressure gradient.

Re	QoI (Exact)	QoI (Drekar)	Adj. Est. Err.	Eff
50	23.4292	23.4077	2.15e-2	1.01
150	70.2875	70.2230	6.55e-2	1.02
500	234.292	234.077	2.18e-1	1.01
1000	468.583	468.154	4.36e-1	1.02

Table 10. Error Estimation for CFD.

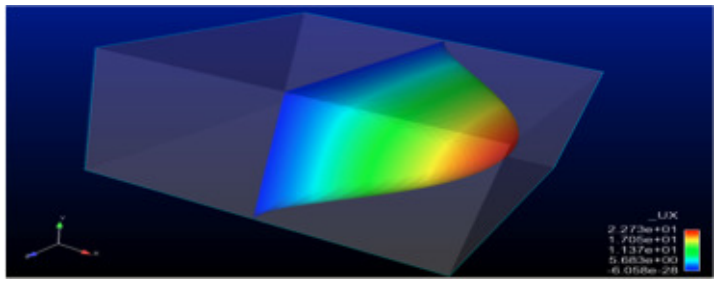

Figure 14. Vx-component of velocity colored by the magnitude.

Re	$dQoI/d\mu$ (Exact)	$dQoI/d\mu$ (Drekar)	Error In Sens. Est.	$dQoI/dG_0$ (Exact)	$dQoI/dG_0$ (Drekar)	Error In Sens. Est.
50	-7.8095	-7.8026	0.09%	-4.686e-2	-4.686e-2	0.0015%
150	-70.285	-70.223	0.09%	-0.14057	-0.14058	0.0014%
500	-780.97	-780.26	0.09%	-0.46858	-0.46859	0.0015%
1000	-3121.0	-3121.0	0.09%	-0.93717	-0.93718	0.0014%

Table 11. Adjoint Sensitivity Analysis for CFD.

Figure 15 shows convergence with mesh spacing for the exact error in the QoI, adjoint error estimate in the QoI (Vx), and the exact relative error in adjoint sensitivity to viscosity ($dQoI/d\mu$) for $Re = 500$. Though convergence is close to the expected value discrepancies may be due to the number of reference values retained in the series, and an issue related to implementation of higher order periodic BCs. Using a laminar flow problem with an analytic solution and choosing a QoI that also has an analytic solution allowed us to verify the accuracy of these adjoint based error estimate and sensitivity analysis. In the next two sections, a much more challenging turbulent flow problem which does not have an analytic solution will be investigated.

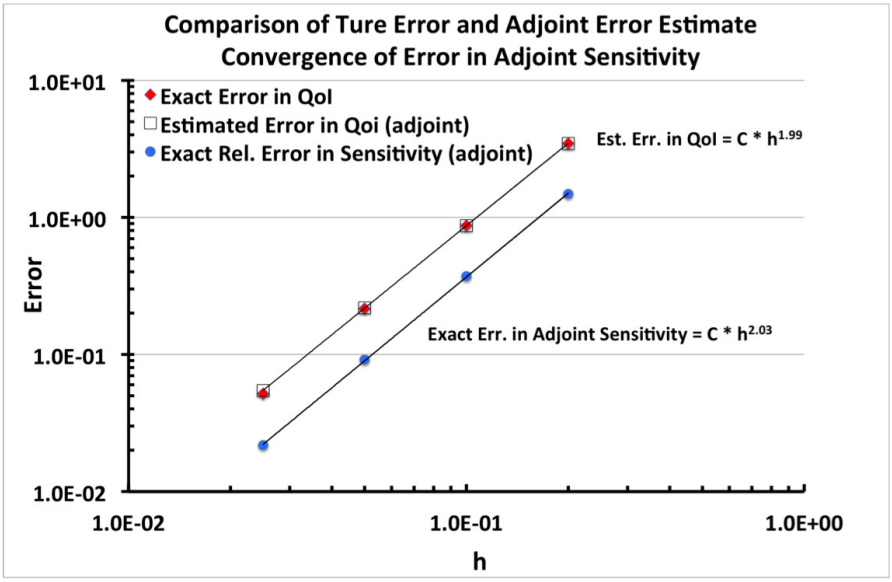

Figure 15. Convergence of exact error in QoI, adjoint based estimated error in QoI, and exact relative error in sensitivity.

4.5.2 Adjoint Sensitivity Analysis for CFD: 3D Turbulent Swirling Flow in Circular Expanding Pipe

The second error estimation and adjoint sensitivity analysis example deals with swirling flow in an axisymmetric sudden expansion tube that was also investigated in an earlier THM CFD milestone report [11], and defined by Pannala and Stagg in an earlier CASL report ([9]). The Reynolds number and swirl number were $Re = 10e4$ and $S = 0.04$ respectively. The Spalart-Allmaras turbulence model was used in these simulations. At this Re and S, a steady-state solution is obtained. The forward solution was obtained using SUPG with Q1 elements and the adjoint problem was solved using Q2 elements. The mesh contained 300,000 elements and the axis of symmetry was along the z-axis. The baseline forward steady-state solution was obtained by pseudo-transient to steady-state time marching, requiring 180 time steps. The maximum time step reached the user-supplied limit $\Delta t_{max} = 10$ and the solution was integrated to 250 time units. Following this psuedo-transient solution, a direct-to-steady-state solution was computed from this initial guess in three Newton steps. Parameter sensitivities were then obtained by reading the forward solution into Drekar and solving the adjoint problem. Forward solutions for the four perturbed solutions ($\mu \pm 1\%, \pm 10\%$) were achieved by solving direct-to-steady-state using the baseline solution as an initial guess. These solutions required two Newton steps for the 1% perturbation in μ and three Newton steps for the 10% perturbation.

In Figure 16 an example taken from a previous milestone is reproduced [11], showing the x-component of velocity contours on a surface of constant z-component of velocity. In this case the Re was the same however, swirl number was ($S = 0.08$). The parameter of interest in these initial numerical sensitivity studies is the dynamic viscosity (μ). Two QoI were computed. The first QoI(1) was the turbulent viscosity in the entire domain;

$$\bar{\hat{\nu}} = \int_{\Omega} \hat{\nu} \, d\Omega \tag{40}$$

and the second QoI(2) was the average cross-stream kinetic energy;

$$KE_{CR} = \int_{\Omega} \frac{1}{2} \rho (u_x^2 + u_y^2) \, d\Omega. \tag{41}$$

A local linear Taylor series model was constructed as a proposed surrogate model for sampling UQ.;

$$q = \bar{q} + \frac{\bar{\partial q}}{\partial p}(p - \bar{p}) \; + \; H.O.T. \tag{42}$$

Table 12 presents the computed values of the two QoI and sensitivity of the two QoI to dynamic viscosity obtained by solving the adjoint problem. Table 13 shows an assessment of using a surrogate of the QoI obtained from the adjoint sensitivity computed in Drekar for assessing UQ in the QoI to the parameter, in this case, μ. The significance of these results have an important impact on UQ. For small variations in parameter space, these results suggest that a surrogate model constructed using Taylor's series and the adjoint sensitivity can be used instead of repeated forward solutions of the perturbed parameter which will greatly reduce the computational cost of the UQ.

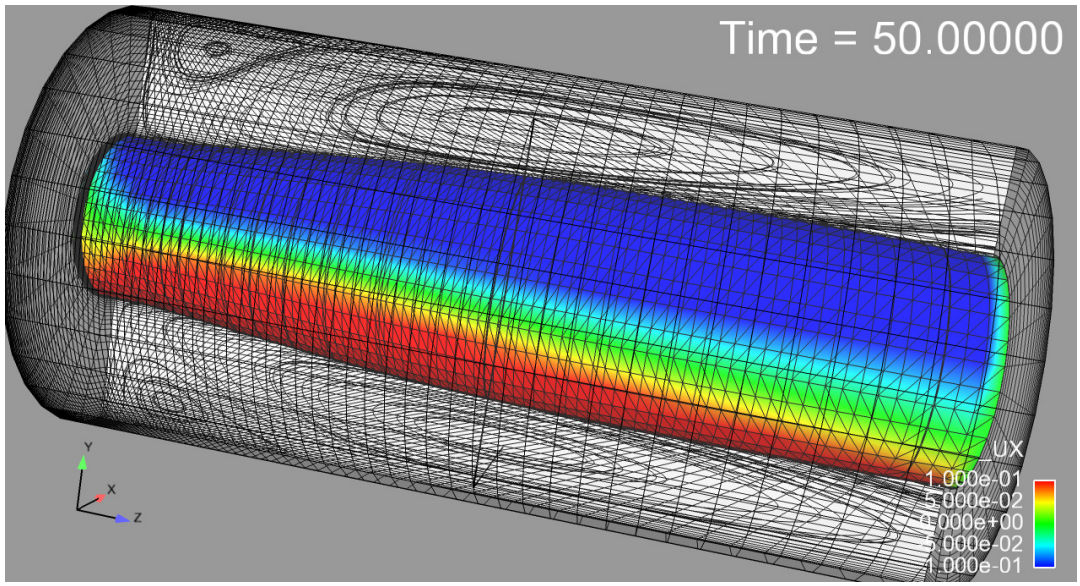

Figure 16. Image of axisymmetric sudden expansion tube at steady-state conditions with $S = 0.08$. Iso-surface of z-component of velocity colored by x-component of velocity, taken from [11].

QoI	QoI computed from Drekar	Adjoint Sensitivity
$\tilde{\hat{\nu}}$	3.866408e+1	-3.74189e+6
KE_{CR}	1.00374e-2	-248.265

Table 12. Estimate of two QoI and adjoint sensitivity for swirling flow in axisymmetric sudden expansion tube.

Dynamic Viscosity (μ)	$\tilde{\hat{\nu}}$ Computed from Drekar	$\tilde{\hat{\nu}}$ Estimated from Adjoint	Rel. Error	KE_{CR} Computed from Drekar	KE_{CR} Estimated from Adjoint	Rel. Error
1.01e-5 (μ+1%)	3.82937e+1	3.82899e+1	0.01%	1.00122e-2	1.00125e-2	0.003%
1.01e-5 (μ-1%)	3.90421e+1	3.90383e+1	0.01%	1.00620e-2	1.00622e-2	0.002%
1.01e-5 (μ+10%)	3.52712e+1	3.49222e+1	1.0 %	9.74522e-3	9.78914e-3	0.450%
1.01e-5 (μ-10%)	4.28242e+1	4.24060e+1	0.97%	1.02835e-2	1.02856e-2	0.020%

Table 13. Error Estimation and Adjoint Sensitivity Analysis for CFD.

4.5.3 Error Estimation 3D Turbulent Swirling Flow in Circular Expanding Pipe

The final example deals with adjoint based error estimation in the same axisymmetric swirling sudden expansion flow. The Reynolds number, swirl number and turbulence model are the same as presented in the previous section. The QoI for this example is the volume integral of the x-component of velocity over half the domain and quantifies to sum extent the strength of the recirculation;

$$\bar{u}_x = \int_{\frac{1}{2}\Omega} u_x \, d\Omega. \tag{43}$$

Half the domain was chosen in order to produce a non-trivial QoI due to axisymmetry. Had the QoI been integrated over the entire domain, negative and positive values would have canceled resulting in zero. Either half could have been chosen or alternatively, the y-component (u_y) of velocity over half the domain could also have been chosen. The swirl problem was run pseudo-transient to steady-state first on a coarse mesh containing $35,964$ elements using 128 cores. The finer mesh containing $287,712$ elements was constructed by uniform refinement of the coarse mesh using STK_Adapt, a Percept tool. The geometry was held constant for the refinement. STK_Adapt interpolates the coarse solution onto the finer mesh which provides a good initial guess for the direct-to-steady-state solver. The fine mesh problem was run on 256 cores. The direct-to-steady-state solver took 9 Newton steps, and an average of 17 Gmres iterations per Newton step (150 total) and a total solution time of 303 seconds to compute. A summary of the computational effort to solve the forward problems is shown in Table 14. Clearly the combination of a coarse initial solution obtained by a pseudo-transient procedure followed by a direct-to-steady-state solution on the fine mesh is very efficient for this problem. Finally, the full computational time for solving the 36K element Q1 stabilized FE nonlinear forward problem (starting from the pseudo-transient solution) in one Newton step and solving the linear adjoint problem for the 36K mesh for the Q2 stabilized FE was 426 seconds on 128 cores.

Mesh	Cores	Δt_{max}	Number steps	CPU time (sec.)	final time (sec.)	CFL (min-max)
35,964	128	10	89 (time steps)	5100	250	9.5-100,000
287,712	256	N.A.	9 (Newton Steps)	303	N.A.	∞

Table 14. Summary of computational effort of error estimation for Swirl flow with $Re_D = 10e4$ and $S = 0.04$.

In Table 15 the results of the Drekar QoI computation and the adjoint error estimate are presented. The computation of the Drekar QoI for the 288K mesh is also presented. Additionally we compute the estimated relative error in the Drekar QoI computation and then based on the finer mesh (288K) QoI we compute the relative error assuming this as the reference value. Using the adjoint for the 36K element mesh Assuming the finer mesh QoI is correct, this result shows that the error estimation based on the adjoint solution is reasonably accurate. If time permits (essen-

tially funding, not CPU time) a more complete study of the accuracy of this error estimate could be obtained and reported.

Mesh	QoI (Drekar)	Error est.	Relative Predicted Error Adjoint	Relative Computed Error from Reference
35,964	0.002054684	0.000380295	18.5%	
287,712	0.002516202			22.5%

Table 15. Error estimation for Swirl flow with $Re_D = 10e4$ and $S = 0.04$.

These results suggest that even on a relatively coarse mesh, the error in a QoI related to a complicated fluid flow problem can be accurately predicted using this methodology.

5 Summary and Observations

In this milestone report the focus has been on two areas of investigation; numerical simulation of the thermal hydraulics of a 3x3 rod/spacer grid reactor core sub-assembly and adjoint based error estimation and parameter sensitivity applied to CFD simulations. These capabilities are highly relevant to the CASL program.

The heat transfer from tube surface to the fluid was validated in a fully developed laminar pipe flow by comparing computed Nusselt numbers to analytically derived values. In a similar way Nusselt numbers were computed from solutions to fully developed turbulent pipe flow at different Reynolds number and compared with empirical derived correlations of Nusselt number. The comparisons show that the slope of the Re_D vs. Nu plot is accurately predicted in the numerical simulations. The results also show a sensitivity to Prt. Numerical simulations bound the correlations if Prt is between 0.5-0.9.

Heat flux at the outflow plane in a 3x3 periodic rod/spacer grid sub-assembly reactor core model was computed from four different mesh solutions. While grid convergent solutions have not yet been achieved, heat flux, eddy viscosity generation and kinetic energy trends are all monotonic. It was argued that the reduction in heat flux as the mesh is refined was due to a reduction in the level of eddy viscosity present as the mesh is refined.

A demonstration of conjugate heat transfer in the same sub-assembly model was demonstrated. The energy equation is linear with respect to the flow variables and so the conjugate problem is solved in two steps. In the first step, flow is solve using pseudo-transient time stepping. In the second step, the fluid flow solution is read into the code as data and the energy equations for both solid and fluid are solved simultaneously.

In the second investigation adjoint based error estimates and parameter sensitives were computed for two flow problems. The first problem was fully developed laminar flow in a rectangular duct which has an analytic solution. The QoI that was chosen also has an analytic solution. Therefore, the accuracy of the error estimates and sensitivities could be assessed. The accuracy was found to quite good.

The second problem involved swirling turbulent flow through an axisymmetric sudden expansion tube. The Spalart-Allmaras model was used in these simulations. Two QoI were selected; the volume integral of eddy viscosity and cross-stream kinetic energy and dynamic viscosity was chosen as a parameter. Sensitivities were computed with respect to viscosity. These sensitivities were used to construct Taylor series based surrogate models of the QoIs. The QoIs were then computed from the surrogate models and compared to computations were the viscosity was perturbed in the same direction and amplitude as for the surrogate models. For both QoIs, the surrogate models were found to be accurate representations of the QoIs. In the future, this approach may be applied to UQ studies.

The final problem involved computing error estimates and for this problem two mesh resolutions were used. The second mesh was obtained by uniformly refining the first mesh. The QoI

was computed on both meshes and the error estimate was computed on the coarse mesh. The error estimate of the QoI computed on the coarse mesh was compared to the relative error between the two mesh resolution predictions of the QoI and were found to be in close agreement.

References

[1] W. Bangerth and R. Rannacher. *Adaptive Finite Element Methods for Differential Equations*. Birkhauser Verlag, 2003.

[2] R. Becker and R. Rannacher. An optimal control approach to a posteriori error estimation in finite element methods. *Acta Numerica*, 10:1–102, 2001.

[3] J. Blazek. *Computational Fluid Dynamics: Principles and Applications*. Elsevier Science LTD, Kidlington, Oxford, UK, 2001.

[4] E.C. Cyr, J.N. Shadid, and T.M. Wildey. Approaches for adjoint-based a posteriori analysis of stabilized finite element methods. *SIAM Journal on Scientific Computing*, submitted.

[5] K. Eriksson, D. Estep, P. Hansbo, and C. Johnson. *Computational differential equations*. Cambridge University Press, Cambridge, 1996.

[6] D. Estep, M. G. Larson, and R. D. Williams. Estimating the error of numerical solutions of systems of reaction-diffusion equations. *Mem. Amer. Math. Soc.*, 146(696):viii+109, 2000.

[7] W.M. Kays and M.E. Crawford. *Convective Heat and Mass Transfer, 2nd Ed.* McGraw-Hill Book Company, 1980.

[8] C. K. G. Lam and K. Bremhorst. A modified form of the $k-\varepsilon$ model for predicting wall turbulence. *ASME, Journal of Fluids Engineering*, 103:456–460, 1981.

[9] S. Pannala and A. Stagg. Casl thm: Cfd benchmarks and test cases. Technical report, OakRidge National Laboratories, 2012.

[10] R.P. Pawlowski, J.N. Shadid, T.M. Smith, E. C. Cyr, and P.D. Weber. Drekar::cfd-a turbulent fluid-flow and conjugate heat transfer code: Theory manual version 1.0. Technical Report SAND2012-2697, Sandia National Laboratories, March 2012.

[11] J. N. Shadid, T. M. Smith, R. P. Pawlowski, E. C. Cyr, and P.D. Weber. Rans cfd simulations for casl thm using drekar::cfd. Technical report, Sandia National Laboratories, October 31 2012.

[12] J. N. Shadid, T. M. Smith, R. P. Pawlowski, E. C. Cyr, P.D. Weber, and D.Z. Turner. Updated initial drekar les cfd simulations for grid-to-rod fretting. Technical report, Sandia National Laboratories, March 31 2012.

[13] J.N. Shadid, A. G. Salinger, R. P. Pawlowski, P. T. Lin, G. L. Hennigan, R.S. Tuminaro, and R. B. Lehoucq. Large-scale stabilized FE computational analysis of nonlinear steady state transport / reaction systems. *Comp. Meth. App. Mechanics and Eng.*, 195:1846–1871, 2006.

[14] T. M. Smith, J. N. Shadid, R. P. Pawlowski, and E. C. Cyr. Reactor core sub-assembly simulations using a stabilized finite element method. *The 14th International Topical Meeting on Nuclear Reactor ThermalHydraulics, NURETH-14, Paper NURETH-14-500 (2011), Toronto, Ontario, Canada*, 2011.

[15] T.M. Smith, J. N. Shadid, R. P. Pawlowski, E. C. Cyr, T. M. Wildey, and P.D. Weber. Initial drekar rans cfd simulations for casl thm. Technical report, Sandia National Laboratories, June 30, 2012.

[16] T.M. Smith, J.N. Shadid, R.P. Pawlowski, E. C. Cyr, P.D. Weber, and R. Garcia. Casl thm cfd review: Fy12 accomplishments. *Presentation*, December 2012.

[17] P. R. Spalart and S. R. Allmaras. A One-Equation Turbulence Model for Aerodynamic Flows. *AIAA Paper 92-0439*, 1992.

[18] P.G. Tucker. Differential equation-based wall distance computation for DES and RANS. *Journal of Computational Physics*, 190:229–248, 2003.

[19] T.M. Wildey, E. C. Cyr, R.P. Pawlowski, J.N. Shadid, and T.M. Smith. Adjoint based a posteriori error estimation in drekar::cfd. Technical Report SAND2012-8910, Sandia National Laboratories, October 2012.

[20] T.M. Wildey, E. C. Cyr, R.P. Pawlowski, J.N. Shadid, and T.M. Smith. A comparison of adjoint and data-centric verification techniques. Technical Report SAND2013-2879, Sandia National Laboratories, April 2013.

DISTRIBUTION:

1	MS 1320	S. Scott Collis, 1440
1	MS 1320	Michael L. Parks, 1442
3	MS 1318	Roger P. Pawlowski, 1444
1	MS 1321	Randall M. Summers, 1444
3	MS 1318	Timothy M. Wildey, 1441
1	MS 1320	Eric C. Cyr, 1426
1	MS 1320	Thomas M. Smith, 1442
1	MS 1321	John N. Shadid, 1444
1	MS 0899	Technical Library, 9536 (electronic copy)

Sandia National Laboratories

CASL-U-2013-0203-001